

Highlights

Reduced-Order Surrogates for Forced Flexible Mesh Coastal-Ocean Models

Freja Høgholm Petersen, Jesper Sandvig Mariegaard, Rocco Palmitessa, Allan P. Engsig-Karup

- Koopman autoencoder extended to forced coastal-ocean systems and compared to POD
- Surrogates evaluated on three real-world hydrodynamic coastal-ocean domains
- Temporal unrolling improves multi-step prediction accuracy
- Koopman surrogates yield -0.64–12% error change vs MIKE 21 compared to observations
- Surrogates are 300–1400x faster than physics-based model

Reduced-Order Surrogates for Forced Flexible Mesh Coastal-Ocean Models

Freja Høgholm Petersen^{a,b}, Jesper Sandvig Mariegaard^a, Rocco Palmitessa^a, Allan P. Engsig-Karup^b

^a*DHI, Agern Allé 5, 2970, Hørsholm, Denmark*

^b*DTU, Department of Applied Mathematics and Computer Science, Bygning 324, 2800, Kgs. Lyngby, Denmark*

Abstract

While POD-based surrogates are widely explored for hydrodynamic applications, the use of Koopman Autoencoders for real-world coastal-ocean modelling remains relatively limited. This paper introduces a flexible Koopman autoencoder formulation that incorporates meteorological forcings and boundary conditions, and systematically compares its performance against POD-based surrogates. The Koopman autoencoder employs a learned linear temporal operator in latent space, enabling eigenvalue regularization to promote temporal stability. This strategy is evaluated alongside temporal unrolling techniques for achieving stable and accurate long-term predictions.

The models are assessed on three test cases spanning distinct dynamical regimes, with prediction horizons up to one year at 30-minute temporal resolution. Across all cases, the Koopman autoencoder with temporal unrolling yields the best overall accuracy compared to the POD-based surrogates, achieving relative root-mean-squared-errors of 0.01–0.13 and R^2 -values of 0.65–0.996. Prediction errors are largest for current velocities, and smallest for water surface elevations. Comparing to in-situ observations, the surrogate yields -0.65% to 12% change in water surface elevation prediction error when compared to prediction errors of the physics-based model. These error levels, corresponding to a few centimeters, are acceptable for many practical applications, while inference speed-ups of 300–1400x enables workflows such as ensemble forecasting and long climate simulations for coastal-ocean modelling.

Keywords:

reduced order model, surrogate, hydrodynamic, proper orthogonal

1. Introduction

Physics-based ocean modelling is a crucial tool in protecting coastal regions from increasing threats from climate change, including sea-level rise and extreme weather events. Accurate prediction of water levels and currents is critical for short-term emergency response planning and long-term coastal infrastructure design (Vieira et al., 1993; Bogaard et al., 2016). Operational forecasting systems typically rely on physics-based hydrodynamic models such as ADCIRC (Luettich et al., 1992), Delft3D (Lesser et al., 2004), or MIKE 21 (DHI, 2024b). Although these models provide high-fidelity simulations, they remain computationally expensive because of the fine spatial resolution and small time steps required to capture hydrodynamic processes. Despite advances in hardware and high-performance computing, this limits the applicability to long climate scenarios and large ensemble simulations, motivating the development of equation-free machine learning based surrogate models that are capable of reproducing the dynamics at a fraction of the computational expense.

While recent advances in deep learning, including neural operators and end-to-end emulation frameworks, have demonstrated impressive performance on idealized or moderately sized domains, their application to large-scale, operational coastal-ocean models remains challenging. In particular, long-horizon stability, robustness under realistic atmospheric and boundary forcing, and interpretability remain key concerns for practical deployment. As a result, equation-free reduced-order surrogate models that explicitly leverage the structure of the underlying dynamics and allow for controlled stability properties continue to be of high relevance in operational ocean modelling.

In this study, we develop and evaluate reduced-order surrogate models for long-term prediction of two-dimensional sea-surface elevation and currents in forced coastal-ocean systems, using three realistic hydrodynamic test cases. Our aim is to achieve substantial speed-up while retaining the physics-based model's skill, when validated against observations. We systematically compare Koopman autoencoder formulations with proper orthogonal decomposition (POD) based surrogates, and we investigate measures to promote temporal stability in the latent-space dynamics.

1.1. Related work

Machine learning has been applied extensively to ocean modelling, ranging from early wave-height forecasting using neural networks (Deo and Sridhar Naidu, 1998) to recent neural-operator-based digital twins for coastal modelling (Jiang et al., 2021). While neural-operator-based approaches demonstrate strong potential for end-to-end emulation, reduced-order surrogates remain attractive for large-scale modelling due to their lower training cost, explicit separation of spatial and temporal components, and fast inference.

Reduced-order models have demonstrated significant potential for accelerating coastal and estuarine simulations. Nogueira et al. (2020) employed a truncated POD-basis to compress over 40,000 grid cells to a latent space of dimension five and then used neural networks to propagate the reduced state. Their surrogate achieved forecasts in a matter of seconds compared with 1.5 hours for the original model. While highly effective, the authors point to limitations of using POD-based surrogates for convection-dominant problems, and they suggest nonlinear autoencoders for future work. More recently, Rivera-Casillas et al. (2025) developed a neural-operator-based surrogate (MITONet) for shallow-water dynamics, reporting 300-600x speed-ups. While MITONet resembles the auto-encoder architectures in this study, the use of neural operators in the latent space greatly increases the number of hyper-parameters to tune, which affects the predictive skills and applicability of the surrogate. However, their study of nonlinear neural autoencoders and temporal operator learning indicates potential of end-to-end training of reduced-order surrogates as opposed to the POD-based surrogates.

Koopman operator theory provides a complementary framework in which nonlinear dynamics are represented by a linear operator acting on an infinite-dimensional observable space. Koopman-inspired approaches aim to learn the observable space in which nonlinear dynamics can be approximated by a linear operator. Convolutional Koopman autoencoders (CKAEs) have been explored for sea-surface temperature and height forecasting (Rice et al., 2021; Brettin et al., 2025). The latter study found that while POD generally provides stronger reconstruction accuracy, CKAEs can yield superior predictive performance and more stable latent-space propagators on a daily time-scale. Such KAE techniques remain under-explored in the context of hydrodynamic applications and hence is investigated in this study.

A critical distinction separates prior Koopman surrogate work from hydrodynamic applications: most existing formulations assume *internal* dynamics, where the system evolves without external inputs. Coastal hydrody-

namics, by contrast, are *forced* systems driven by time-varying wind fields, atmospheric pressure, and boundary conditions e.g. from coarser global models. Proctor et al. (2018) extended Koopman operator theory to systems with control inputs, and they establish a formulation for inputs that have their own dynamics. Shi and Meng (2022) introduced a deep-learning architecture that uses a separate neural network to handle control inputs in their Koopman operator. To our knowledge, forced system formulations have not yet been applied to coastal-ocean surrogate models operating under realistic meteorological forcing.

Beyond architecture, recent work has explored loss formulations that promote desirable operator properties, such as forward–backward consistency (Azencot et al., 2020), temporal consistency (Nayak et al., 2025), asymptotic stability constraints (Lortie et al., 2024), or trajectory-unrolled training (Morton et al., 2019; Otto and Rowley, 2019; List et al., 2024). In this work we examine two such strategies, stability regularization and temporal unrolling, and evaluate their impact on both POD-based and Koopman-based surrogates.

1.2. Contributions

This study contributes to advancing the state of reduced-order surrogate modelling for coastal hydrodynamics in four ways: 1) We develop and evaluate a Koopman autoencoder surrogate formulation for forced coastal hydrodynamics, explicitly incorporating atmospheric and boundary forcing relevant to operational ocean models. 2) We provide a systematic comparison of Koopman-based and POD-based reduced-order surrogates for sea-surface elevation and depth-averaged currents to illuminate tradeoffs between performance and skill. 3) We assess the impact of stability-promoting training strategies, including eigenvalue regularization and temporal unrolling, on long-term predictive skill and robustness. 4) We demonstrate the generalizability and limitations of these approaches through application to three real-world hydrodynamic cases, highlighting practical trade-offs between model complexity, accuracy, and stability, as well as cost of implementation.

The remainder of the paper presents the surrogate formulations, and training strategies in Section 2, the three hydrodynamic test cases in Section 3, followed by a comparative evaluation of accuracy, stability, and speed against both physics-based simulations used for training and observational data in Section 4. Section 5 discusses the results and proposes future directions followed by a conclusion in Section 6.

2. Methodology

2.1. Flowmap formulation

The physics-based models considered in this study are numerical hydrodynamic models that solve the shallow-water equations (SWE), i.e. a set of equations derived by depth-averaging the Navier–Stokes equations, on a spatial domain Ω . With a spatial discretization on an unstructured mesh $\Omega_h \approx \Omega$, the mesh element values of the model state variables (e.g. surface elevations and horizontal velocities) are collected in $\mathbf{x} \in \mathbb{R}^{N_x}$. Under forcings $\mathbf{u} \in \mathbb{R}^{N_u}$, the state evolves in discrete time according to a nonlinear temporal mapping $\mathcal{F}_\beta : \mathbb{R}^{N_x} \times \mathbb{R}^{N_u} \rightarrow \mathbb{R}^{N_x}$,

$$\mathbf{x}_{k+1} = \mathcal{F}_\beta(\mathbf{x}_k, \mathbf{u}_k), \quad k = 1, \dots, N_T, \quad (1)$$

where k denotes the discrete time index of time-increments Δt , assumed constant, N_T is the total number of time steps, and β represents the model parameters, such as bottom-friction coefficients in coastal-ocean applications. Throughout this study, the external forcing \mathbf{u} (e.g. wind, pressure and boundary conditions) is assumed known over the prediction horizon and prescribed from external data sources. While the underlying physics-based model may use dynamic time-stepping, the formulation (1) corresponds to the form of the output data, where the time-step is assumed constant.

The surrogate model in this study can be described as an approximation to the flowmap, denoted $\tilde{\mathcal{F}}_\beta \approx \mathcal{F}_\beta$. The dimensionality of both the states and forcings is reduced through an autoencoder mapping, and the latent variables are propagated temporally,

$$\mathbf{x}_{k+1} \approx \tilde{\mathcal{F}}_\beta(\mathbf{x}_k, \mathbf{u}_k, \mathbf{u}_{k+1}) = \Phi_D(\mathcal{M}(\Phi_E(\mathbf{x}_k), \Psi_E(\mathbf{u}_k), \Psi_E(\mathbf{u}_{k+1}))), \quad (2)$$

$$k = 1, \dots, N_T,$$

where $\Phi_E : \mathbb{R}^{N_x} \rightarrow \mathbb{R}^{\tilde{N}_x}$ and $\Phi_D : \mathbb{R}^{\tilde{N}_x} \rightarrow \mathbb{R}^{N_x}$ are the encoder and decoder for the states, with $\tilde{N}_x \ll N_x$, $\Psi_E : \mathbb{R}^{N_u} \rightarrow \mathbb{R}^{\tilde{N}_u}$, $\tilde{N} \ll N$, is an encoder for the forcings, and $\mathcal{M} : \mathbb{R}^{\tilde{N}_x} \times \mathbb{R}^{2\tilde{N}_u} \rightarrow \mathbb{R}^{\tilde{N}_x}$ is the temporal propagator in the latent space of reduced dimension. The forcings both at time k and $k + 1$ are used in the temporal propagator for improved accuracy, leading to the indicated size of \mathcal{M} . Because the surrogate uses identical inputs and outputs as the physics-based model, it can work as a direct replacement in ensemble forecasting, probabilistic studies, and long climate simulations. In the general formulation (2), the autoencoders and the propagator can be

linear or nonlinear. In the following sections, we will look into two special cases of this surrogate, namely a Koopman autoencoder and a POD-based surrogate.

2.2. Koopman autoencoder surrogate

Koopman operator theory is concerned with establishing a Koopman invariant subspace of infinite dimensions, where nonlinear dynamics are represented by a linear infinite-dimensional operator. This idea has inspired the use of neural networks for learning subspaces that are finite-dimensional approximations to the Koopman invariant subspace, where the dynamic can be assumed linear. Having a globally linear latent operator as opposed to locally linearizing nonlinear dynamics allows for exact analyses in applications such as control problems (Proctor et al., 2018; Kaiser et al., 2021). In the current application, the advantage of a linear operator is that analysis of asymptotic stability is straight-forward and exact through computation of eigenvalues. Since the operator acts in a reduced space, the computation of eigenvalues is of negligible cost. Section 2.2.1 introduces the finite-dimensional approximation of the Koopman Operator, Section 2.2.2 introduces the approximation for forced systems, and Section 2.2.3 links this to the general surrogate formulation (2).

2.2.1. Koopman operators for autonomous systems

For a nonlinear, discrete-time dynamical system, $\mathbf{z}_{k+1} = \mathbf{F}(\mathbf{z}_k)$, where \mathbf{z} exists on a manifold $M \subset \mathbb{R}^m$, Koopman operator theory (Koopman, 1931; Mezić, 2005; Brunton et al., 2016) describes an infinite dimensional operator, \mathcal{K} , that acts on an observable function g

$$\mathcal{K}g(\mathbf{z}_k) = g(\mathbf{F}(\mathbf{z}_k)) = g(\mathbf{z}_{k+1}). \quad (3)$$

Following the argument by Azencot et al. (2020), the infinite-dimensional \mathcal{K} can be approximated by a finite-dimensional encoding C that preserves most of the dynamics,

$$C = \mathcal{X} \circ \mathcal{K} \circ \mathcal{X}^{-1}, \quad C \in \mathbb{R}^{\kappa \times \kappa}, \quad (4)$$

where $\kappa \in \mathbb{Z}_{>0}$ and $\kappa < \infty$, and \mathcal{X} and its inverse are the encoder/decoder structure that extracts most important features from \mathcal{K} . Inserting this transformation in (3) yields the important result

$$\mathcal{X}^{-1} \circ C \circ \mathcal{X}(g(\mathbf{z}_k)) \approx g \circ \mathbf{F}(\mathbf{z}_k). \quad (5)$$

This means that if we can determine a meaningful encoding \mathcal{X} of the observables g , we can represent the dynamics in the observable space using the finite-dimensional, linear mapping C .

2.2.2. Koopman operators for forced systems

Proctor et al. (2018) generalize Koopman theory to dynamical systems with control. For open-loop control, where the input is a time-varying exogenous forcing term, \mathbf{f}_k , the observable function g acts on the state and the input. For a flowmap formulation such as (1), the Koopman step is $\mathcal{K}g(\mathbf{z}_k, \mathbf{f}_k) = g(F(\mathbf{z}_k, \mathbf{f}_k))$. If the Koopman operator is square, this formulation propagates both the state and the forcing input, in the case that the forcing is unknown. However, in our case, the forcing is assumed known, and \mathcal{K} is therefore not square, and it propagates only \mathbf{z} .

Introducing a finite-dimensional encoding, \mathcal{X}_f , such that $C_f = \mathcal{X}_f \circ \mathcal{K} \circ \mathcal{X}_f^{-1}$, for $C_f \in \mathbb{R}^{\kappa_1 \times \kappa_2}$, we get the forced formulation of the finite-dimensional approximation of the Koopman operator

$$\mathcal{X}_f^{-1} \circ C_f \circ \mathcal{X}_f(g(\mathbf{z}_k, \mathbf{f}_k)) = g(F(\mathbf{z}_k, \mathbf{f}_k)). \quad (6)$$

In this study, we consider the practical case of prescribed external forcing. The surrogate therefore propagates only the system state, while the forcing enters as a known exogenous input at each time step. No attempt is made to model or predict the forcing dynamics.

2.2.3. Koopman autoencoder surrogate model

In the context of this study, the states, \mathbf{z}_k , are *observed* on a flexible mesh of Ω_h . Considering the general surrogate formulation (2), this means $(\mathbf{x}_k, \mathbf{u}_k) \equiv g(\mathbf{z}_k, \mathbf{f}_k)$. Correspondingly, $\mathcal{M} \equiv C_f$, $(\Phi_E, \Psi_E) \equiv \mathcal{X}_f$ and $\Phi_D \equiv \mathcal{X}_f^{-1}$. The encoder/decoder structure that we seek is approximated using different types of neural networks, and the matrix C_f in (6) can similarly be approximated e.g. using neural networks or ordinary least squares (OLS) regression.

The encoders are trained to map the state variables, observed on the mesh, to a latent space in which the temporal evolution can be approximated by a linear operator. This is achieved through end-to-end training of the encoders, decoders and the matrix C_f as visualized in Figure 1a. The training aims at solving the minimization problem using the mean squared

error (MSE)

$$\begin{aligned} \arg \min_{\Phi_E, \Phi_D, \Psi_E, \mathbf{C}_f} \mathcal{L} &= \mathcal{L}_{pred} + \mathcal{L}_{recon} \\ &= \text{MSE}(\mathbf{x}_{k+1}^{pred}, \mathbf{x}_{k+1}^{true}) + \text{MSE}(\mathbf{x}_k^{recon}, \mathbf{x}_k^{true}), \end{aligned} \quad (7)$$

where $\mathbf{x}_{k+1}^{pred} = \Phi_D \circ C_f(\Phi_E(\mathbf{x}_k), \Psi_E(\mathbf{u}_k), \Psi_E(\mathbf{u}_{k+1}))$ is the propagation through the KAE, and $\mathbf{x}_k^{recon} = \Phi_D(\Phi_E(\mathbf{x}_k))$ is the state reconstruction with the autoencoder. The MSE is defined as $\text{MSE}(A, B) = 1/(NT) \sum_{i,j} (A - B)_{i,j}^2$, $A, B \in \mathbb{R}^{N \times T}$, where N is the number of spatial elements and T is the number of time steps. The loss-term separates the reconstruction and the prediction loss, such that the autoencoders only reconstruct the data and avoid unintentionally encoding dynamics of the variables.

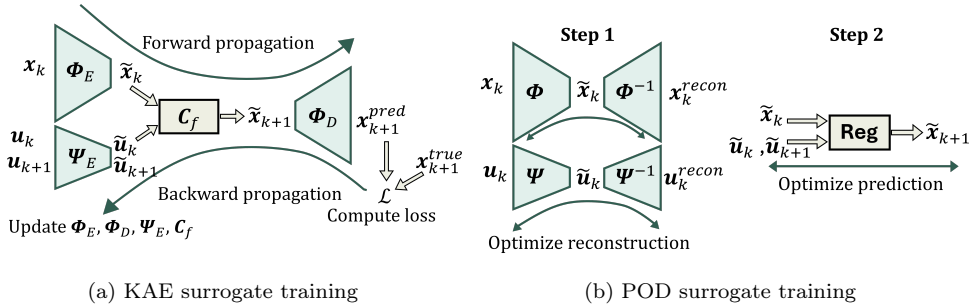


Figure 1: (a) Training of the Koopman-based Autoencoder in an end to end setting, and (b) training of POD surrogate in two steps: 1) Optimize the reconstruction loss for encoding and decoding, 2) optimize prediction loss.

The state variables and the forcings are encoded and decoded separately, because the properties of the states and the forcings are different. For instance, the wind field of the forcings could require nonlinear layers, whereas the state variables in the hydrodynamic data can often be reconstructed with simple linear neural networks. Thus, the separation allows for a simpler surrogate with fewer parameters.

2.3. POD-based surrogate model

Proper Orthogonal Decomposition (POD), also commonly referred to as Empirical Orthogonal Functions (EOFs) in oceanography and as Principal Component Analysis (PCA) in statistics and machine learning, is a well-established technique for reduced-order modelling of geophysical flows. POD

determines an orthogonal basis whose directions maximize the variance of the data, representing a time-series of snapshots of state information, upon projection onto the basis. The spatial POD modes correspond to the left singular directions of the covariance matrix, $\mathbf{X}\mathbf{X}^T$, when \mathbf{X} contains discrete data points,

$$\mathbf{X} = \begin{bmatrix} x_{1,1} & x_{1,2} & \cdots & x_{1,N_T} \\ x_{2,1} & x_{2,2} & \cdots & x_{2,N_T} \\ \vdots & \vdots & \ddots & \vdots \\ x_{N_x,1} & x_{N_x,2} & \cdots & x_{N_x,N_T} \end{bmatrix}.$$

A latent space can be obtained by truncating the resulting spatial POD basis, such that only the first r singular vectors are used to span the latent space. Generally, the singular value decomposition (SVD) used for obtaining the matrix decomposition of the snapshot matrix \mathbf{X} is computationally expensive, so the randomized SVD-algorithm Halko et al. (2010) is used in this study for computational efficiency.

A reduced-order surrogate model for hydrodynamic simulations can be constructed using POD for compression and a regression model for temporal propagation. Figure 1b illustrates the two components of the POD-based surrogate being trained separately. Compared to the KAE, this means that the POD-model makes no assumptions about the dynamic in the latent space.

In this study, two different regression models are tested: linear regression (LR) and a multi-layer perceptron (MLP). The POD+LR model resembles the KAE, except for the separated training. The POD+MLP model, however, allows for nonlinear temporal propagation, since the POD does not assume a latent space with linear dynamic.

2.3.1. Temporal propagators

The linear regression has the form

$$\tilde{\mathbf{x}}_{k+1} = \mathbf{A} \begin{bmatrix} \tilde{\mathbf{x}}_k \\ \tilde{\mathbf{u}}_k \\ \tilde{\mathbf{u}}_{k+1} \end{bmatrix}, \quad (8)$$

where $\mathbf{A} \in \mathbb{R}^{\tilde{N}_x \times (\tilde{N}_x + 2\tilde{N}_u)}$ is the coefficient matrix of a linear flowmap formulation, and the \sim denotes latent variables after POD projection. \mathbf{A} can be

determined using an ordinary least squares (OLS) fit that solves the optimization problem with the closed-form solution

$$\arg \min_{\mathbf{A}} \|\tilde{\mathbf{X}}' - \mathbf{AB}\|^2, \\ \mathbf{A} = (\mathbf{B}^T \mathbf{B})^{-1} \mathbf{B}^T \tilde{\mathbf{X}}', \quad \mathbf{B} = \begin{bmatrix} \tilde{\mathbf{X}} \\ \tilde{\mathbf{U}} \\ \tilde{\mathbf{U}}' \end{bmatrix}, \quad (9)$$

where $\tilde{\mathbf{U}} = [\tilde{\mathbf{u}}_1, \tilde{\mathbf{u}}_3, \dots, \tilde{\mathbf{u}}_{N_T-1}]$, $\tilde{\mathbf{X}} = [\tilde{\mathbf{x}}_1, \tilde{\mathbf{x}}_2, \dots, \tilde{\mathbf{x}}_{N_T-1}]$ and $\tilde{\mathbf{X}}' = [\tilde{\mathbf{x}}_2, \tilde{\mathbf{x}}_3, \dots, \tilde{\mathbf{x}}_{N_T}]$. The prime denotes a time-shifted matrix, and hence, the linear regression optimizes the one-step prediction error.

Apart from the OLS, another option is to use a simple neural network without hidden layers or activation functions. It can be fitted using back-propagation and an optimization algorithm, which aims at minimizing the MSE loss:

$$\arg \min_{\mathbf{A}} \mathcal{L}_{pred} = \text{MSE}(\tilde{\mathbf{X}}', \mathbf{AB}). \quad (10)$$

The purpose of this form of the linear regression is that it is possible to add different regularization terms to the loss as described in Section 2.4.

A multi-layer perceptron (MLP) is a feed-forward neural network with a number of hidden layers and hidden units, and which uses rectified linear unit (ReLU) activation functions. Smooth activation functions (e.g. SiLU) were tested with similar performance, but they may be preferable for physics-informed extensions. Similar to the linear regression, the MLP is trained on one-step predictions given the previous state and the next forcing values.

2.4. Loss regularization and temporal unrolling

Both types of surrogates are usually trained based on one-step predictions. However, the surrogates are supposed to be applied for long-term predictions of lengths from a few days to several years. One-step training can yield propagators whose errors compound rapidly, leading to numerical instability or drift. We investigate two complementary remedies: eigenvalue regularization to enforce stability constraints on the linear propagators, and temporal unrolling to expose training to multi-step error accumulation.

For eigenvalue regularization, a loss-term is added to the objective functions (7) and (10), such that the loss is penalized if any eigenvalue of the

system matrix is larger than 1. Specifically, the linear propagator in (8) has the form $\mathbf{A} = [\mathbf{A}_{X,X'}, \mathbf{A}_{U,X'}, \mathbf{A}_{U',X'}]$, where the subscript (X, X') indicates that X' is explained by input X and similarly for U on X' and U' on X' . Similarly for the Koopman approximation C_f . The eigenvalue regularization is then based on the eigenvalues of the square matrix $\mathbf{A}_{X,X'}$, describing the *inner dynamics*, such that the optimization problem for the KAE and POD-based surrogates is

$$\arg \min_{\theta} \mathcal{L} = \alpha_{pred} \mathcal{L}_{pred} + \alpha_{recon} \mathcal{L}_{recon} + \alpha_{eig} \sum_i^{\tilde{N}_x} \text{ReLU}(|\lambda(\mathbf{A}_{X,X'})_i| - 1),$$

where $\alpha_i \in [0, 1]$, $i = [pred, recon, eig]$, are regularization weights, and θ are the surrogate parameters. For the POD-based surrogates, $\alpha_{recon} = 0$. The eigenvalue regularization is zero when all eigenvalues within the unit circle, and it is equal to the eigenvalue magnitude when outside or on the unit circle. Eigenvalues within unit indicates asymptotic stability in the temporal propagator, and as long as the external forcing input is bounded, the dynamic of the temporal propagator will be bounded. We note that for systems with sustained oscillatory modes, such as tidal dynamics, eigenvalues near the unit circle ($|\lambda| \approx 1$) are physically meaningful. The regularization above does not penalize eigenvalues below unity, preserving the model's ability to represent neutrally stable oscillations.

The eigenvalue regularization promotes temporal stability, but it does not guarantee accuracy, and it only works in linear temporal models. Temporal unrolling is implemented for both linear and nonlinear propagators. During training, the loss is computed based on several *unrolled* time-steps. That is, the temporal propagator is applied auto-regressively for a number of time-steps, and the model parameters are updated based on gradients back-propagated through all of the unrolled time-steps. For the temporal mapping \mathcal{M} in (2), this means that the prediction loss is computed as a sum of errors over the unrolled trajectory in latent space,

$$\mathcal{L}_{pred} = \sum_{s=1}^{N_{TU}} \text{MSE}(\mathcal{M}^s(\tilde{\mathbf{x}}_k, \tilde{\mathbf{u}}_k, \tilde{\mathbf{u}}_{k+1}), \tilde{\mathbf{x}}_{k+s}),$$

where N_{TU} is the number of unrolled time steps, and \mathcal{M}^s corresponds to s consecutive evaluations of the temporal propagator given an initial value on the trajectory.

The assumption is that exposing the parameter optimization to longer sequences will allow it to explore more of the transient dynamics, which will reduce the data-distribution shift between training and test data. The challenge is to balance the number of unrolled time-steps, since the backpropagated gradients can diverge with too long unrolled sequences (List et al., 2024).

2.5. Computational complexity

The POD-based surrogates and the KAE-surrogates differ largely in terms of computational complexity. The POD computation with the randomized SVD has computational complexity $\mathcal{O}(N_x N_T \log(k))$ for finding the k dominant components in a matrix of size $N_x \times N_T$ (Halko et al., 2010). The OLS fit (9) has complexity $\mathcal{O}(N_T \tilde{N}_{x,u}^2)$ (for least squares fit with QR-factorization) where $\tilde{N}_{x,u} = \tilde{N}_x + 2\tilde{N}_u$ is the latent space dimension for the forcings and states together. This work is carried out in the offline phase, and in the online phase, the compression and decompression of the state and forcings requires $\mathcal{O}(N_x \tilde{N}_x + N_u \tilde{N}_u)$ floating point operations (FLOP), and a linear operator requires $\mathcal{O}(\tilde{N}_x \tilde{N}_{x,u})$ FLOP for a one step prediction. Since $\tilde{N}_x \ll N_x$ and $\tilde{N}_u \ll N_u$, the overall complexity of a one step prediction with POD-based surrogate simplifies to $\mathcal{O}(N_x + N_u)$. The complexity is the same for a MLP-based temporal propagator, except for the offline phase being more computationally expensive due to iterative optimization of parameters.

For the KAE, the offline phase is an iterative process, where the optimization of parameters in the autoencoder is based on updates using loss gradients. In each iteration (epoch), the the optimization requires forward passes through the network for computation of losses and backward passes for computation of gradients. The forward pass of one training sample in a KAE with purely linear autoencoder has complexity $\mathcal{O}(N_x + N_u)$, and the backpropagation is $\mathcal{O}(N_x + N_u)$. The overall time complexity then depends on the number of training samples N_T and the number of epochs needed for the training N_{epoch} , such that the overall complexity of the offline phase is $\mathcal{O}(N_{epoch} N_T (N_x + N_u))$, ignoring the operations in the latent space since the latent space is assumed very small relative to N_x and N_u . For nonlinear layers, e.g. of size $(N_{xl1}, N_{xl2}, \dots)$ in the state autoencoder, the complexity for a forward and backward pass is $\mathcal{O}(N_{epoch} N_T (N_x N_{xl1} + N_{xl1} N_{xl2} + \dots + N_u))$. Increasing layers simply lead to increased complexity. Since many epochs are often required, the computational complexity of the offline phase of the

KAE is much more expensive than that of the POD. The use of batch-parallelizations can improve the wall-clock time. The online phase of the KAE for arbitrary layers in the autoencoders, corresponds to a forward pass, namely $\mathcal{O}(N_x N_{xl1} + N_{xl1} N_{xl2} + \dots + N_u N_{ul1} + N_{ul1} N_{ul2} + \dots)$ for one time-step.

Temporal unrolling and eigenvalue regularization adds to the time complexity. For POD-based models, these are negligible compared to the compression and decompression parts, since they are performed in the latent space. The eigenvalue decomposition is $\mathcal{O}(\tilde{N}_x^3)$. For KAE, the eigenvalue decomposition is also only computed in the latent space and therefore negligible, however, the temporal unrolling has to be back-propagated through the encoders. The temporal unrolling itself is $\mathcal{O}(\tilde{N}_x \tilde{N}_{x,u})$, but the backpropagation through time treats each time-step as a layer in the neural network, meaning that the backpropagation has complexity $\mathcal{O}(N_{TU}(N_x + N_u))$ for a linear autoencoder, where N_{TU} is the number of unrolled time-steps. Increasing the number of layers increases the time-complexity similar to above. Space complexity also scales with N_{TU} .

2.6. Variable-separated autoencoders

For the present application, the states and forcings consist of several variables, which have different dynamics. Specifically, the state vector \mathbf{x}_k consists of three state variables: surface elevations (S), and the depth-averaged current velocity consisting of its eastward component U , and northward component V . The forcing vector \mathbf{u}_k consists of boundary conditions (S_{BC} , U_{BC} , V_{BC}), that is, S , U and V imposed on element faces on the open boundary, and 10-metre wind velocity components (W_U , W_V) and mean sea level pressure (P).

Since the dynamics of the different variables are remarkably different, e.g. S is very smooth, while U and V are relatively non-smooth, it can make sense to introduce separate autoencoders. Figure 2 shows an example of a concatenated autoencoder structure where all state variables are encoded together, and a separated architecture where S is encoded separately from U and V . Similar adjustments of the autoencoders can be made for the forcing variables. Differentiating between dynamics, allows for different choices of architectures e.g. mixing POD with neural networks, or using convolutional neural networks for gridded data. Further, the separated architecture uses fewer parameters for the same latent space dimension. Section 4, will present the chosen autoencoder configurations.

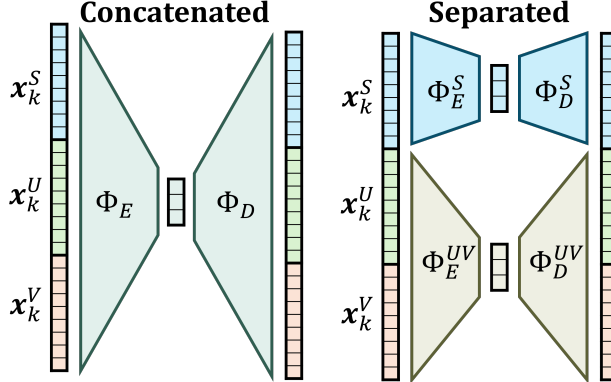


Figure 2: Graphical representation of autoencoders.

2.7. Summary and implementation of methods

Surrogates are abbreviated in the following way: PODLR (POD with OLS linear regression), PODLRt (POD with backpropagation based training of linear regression), PODMLP (POD with multi-layer-perceptron), KAE (Koopman autoencoder), LKAE (KAE with linear autoencoder). Further, the suffix 'eig' and 'TU' can be added, to denote eigenvalue regularization and temporal unrolling, respectively.

All experiments are performed in Python 3.12. The POD is implemented using the Scikit-learn (Pedregosa et al., 2011) (version 1.6) implementation of principal component analysis. The temporal propagator for the PODLR is implemented using Darts (Herzen et al., 2021), which is a useful library for handling lagged and lead variables. The remaining propagators and neural network based autoencoders are implemented using Pytorch (Paszke et al., 2019). All models are trained on an NVIDIA L4 GPU with 24 GB memory and 8 CPUs through the Lightning AI platform (Lightning AI, 2025). The neural networks are trained using the Adam or AdamW optimizer (Kingma and Ba, 2017; Loshchilov and Hutter, 2017; Pytorch, 2025a).

For each surrogate architecture, a hyper-parameter optimization is performed using Optuna (Akiba et al., 2019), which uses a TPE (Tree-structured Parzen Estimator) algorithm for automatically sampling hyper-parameters during the optimization. The optimization aims at selecting the hyper-parameters that minimizes the validation error in an autoregressive forecast. The resulting parameters are shown in Appendix B.2. Only the best-performing models per class are reported.

3. Data and experimental setup

This section describes the simulation data used to train and evaluate surrogate models. We employ three coastal-ocean domains spanning distinct dynamical regimes, allowing assessment of surrogate generalizability across conditions encountered in operational coastal modelling.

All surrogates are trained using physics-based simulation data generated numerically from the MIKE 21 Flow Model FM (DHI, 2024b). MIKE 21 is a widely used commercial hydrodynamic model that solves the two-dimensional shallow water equations (SWE) using a cell-centered finite volume discretization on a flexible mesh. The model outputs surface elevation (S) and depth-averaged velocity components (U, V) at 30-minute intervals on all mesh elements. Forcing inputs include 10-metre wind velocity components and mean sea level pressure as well as S, U and V on lateral open boundaries.

3.1. Test cases

Table 1 summarizes the three cases representative for coastal-ocean applications of realistic complexity. The number of mesh elements indicates the spatial dimension of the data, meaning that the surrogate will have spatial dimension $N_x = 3 \cdot N_{elements}$, since there are three state variables represented on the mesh. The forcing data is summarized in Table A.5 in Appendix A. The bathymetries of the cases are visualized in Figure 3, where the black dots mark measuring stations, which will be used for comparing the surrogate model results to observation data. An overview of the measurement stations is found in Table A.6 in Appendix A. The model setups and output data are publicly available for two of the cases, Øresund and Southern North Sea (DHI, 2024a, 2025).

The temporal train and test split is visualized in Figure 4, where the time series of the surface elevation is shown for a single spatial point and the testing period is marked by a gray background. During training, the last 10% of the time-steps in the training data is used as validation data for early stopping. With this choice of training and test split, the models are exposed to periods with a large variation and to calmer periods.

3.1.1. Case 1: Øresund

The Øresund strait between Denmark and Sweden constitutes the first case study DHI (2024a). The area has a minor tidal range (10-20 cm) and the dynamics are dominated by the surge introduced through the boundaries

Table 1: Overview of simulation domains and time periods available for the three cases.

	Øresund	Southern North Sea	Adriatic Sea
Train period	Jan-Dec 2021	Jan-Dec 2022	Jan-Aug 2021
Test period	Jan-Dec 2022	Jan-Dec 2023	Sep-Dec 2021
Mesh elements	3320	8533	28158
Area [km^2]	2000	240 000	130 000

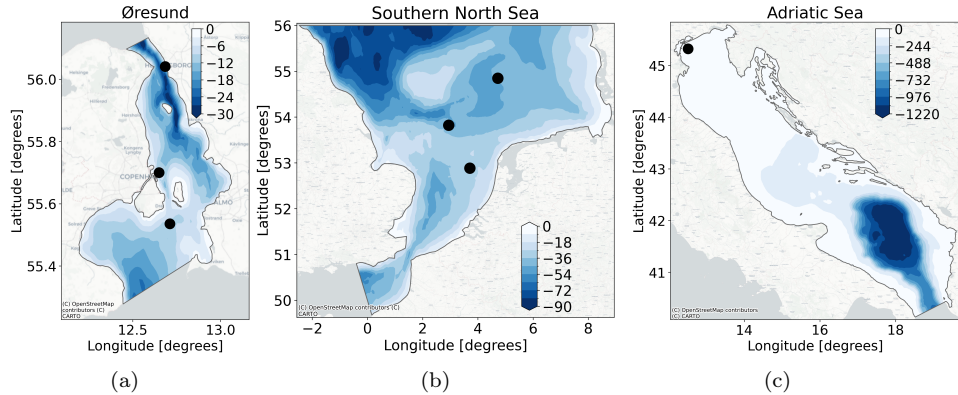


Figure 3: The domains and the bathymetries of the three cases, Øresund (a), Southern North Sea (b), and Adriatic Sea (c). The dots indicate the location of measuring stations.

from wind- and pressure-driven flow, as well as density driven circulation and seiching in the Baltic Sea.

3.1.2. Case 2: Southern North Sea

The second test case is a model of the Southern North Sea (DHI, 2025) spanning from the English Channel along the Southern and Eastern English coast, part of the Northern French coast, and the coasts of Belgium, the Netherlands, Northwest Germany, and Southwest Denmark. This large shelf sea exhibits strong semi-diurnal tides, with spring ranges exceeding 5 metres in the eastern English Channel. The model represents a *simplified* version of the work performed by DHI for the Rijksdienst voor Ondernemend Nederland (RVO) (DHI, 2023). The domain has an open boundary to the North and an open boundary to the South in the English channel.

3.1.3. Case 3: Adriatic Sea

The third test case is the Adriatic Sea located between the Italian Peninsula and the Balkan Peninsula. The test case is based on the operational

model used for a Decision Support System that protects Venice against flooding (DHI, 2024c). The semi-enclosed basin dynamics combine moderate tidal forcing, strong wind-driven circulation from the Bora and Sirocco winds, and resonant basin oscillations (seiching) that can amplify water levels at the northern end. This phenomenon causes Venice’s acqua alta flooding events (DHI, 2024c).

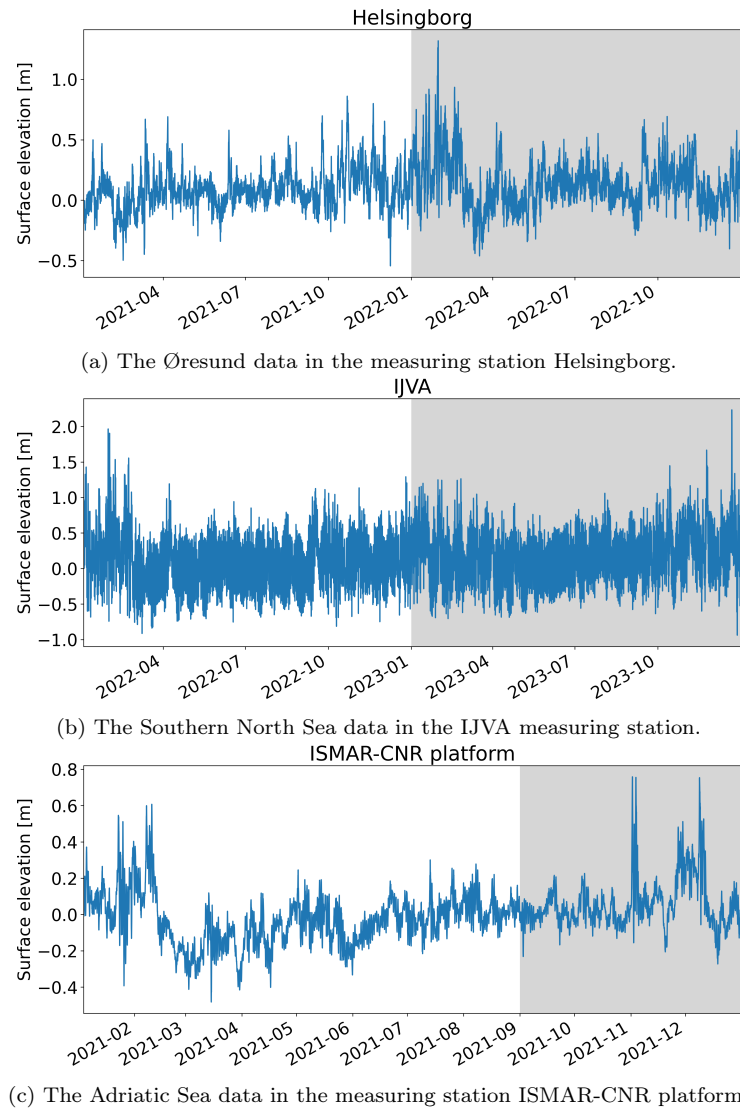


Figure 4: Example timeseries of the surface elevation data used for training the surrogates.

In the present simulation setup, tidal forcing has been removed to isolate the meteorologically-driven dynamics. This detided configuration focuses the surrogate learning task on the more challenging aperiodic wind and pressure response, without the regular tidal signal that aids prediction in the North Sea case. The Adriatic case thus provides the most demanding test of surrogate capability, combining complex resonant dynamics, the largest mesh, and a shorter training period.

3.2. Evaluation metrics

The surrogate aims at emulating the physics-based model and to evaluate its performance on the test period, the correlation coefficient, R^2 , the root-mean-squared-error (RMSE) as well as the RMSE relative to the value range are used. Hence, the MIKE 21 simulation data is assumed the ground truth when evaluating the R^2 by

$$R^2 = 1 - \frac{SS_{res}}{SS_{tot}},$$

where the sum of squared residuals $SS_{res} = \sum_{i=1}^{N_x} \sum_{k=1}^{N_T} (x_{k,i} - \hat{x}_{k,i})^2$ and the total sum of squares $SS_{tot} = \sum_{i=1}^{N_x} \sum_{k=1}^{N_T} (x_{k,i} - \bar{x})^2$, with \bar{x} being the mean value. Similarly for the spatio-temporal RMSE,

$$RMSE(\hat{\mathbf{x}}, \mathbf{x}) = \sqrt{\frac{1}{N_T N_x} \sum_{k=1}^{N_T} \sum_{i=1}^{N_x} w_i (x_{k,i} - \hat{x}_{k,i})^2},$$

where w_i consists of the spatial mesh element areas.

The relative RMSE is normalized by the spatial range of values of the physics-based simulation,

$$Rel. RMSE(\hat{\mathbf{x}}, \mathbf{x}) = \frac{1}{N_x} \sum_{i=1}^{N_x} \frac{\sqrt{\frac{1}{N_T} \sum_{k=1}^{N_T} w_i (x_{k,i} - \hat{x}_{k,i})^2}}{\max_{k \in 1, \dots, N_T} x_{k,i} - \min_{k \in 1, \dots, N_T} x_{k,i}}. \quad (11)$$

That is, the relative RMSE is the mean of the RMSE across time in each mesh element divided by the range of values in that specific element, in order to take local variability into account.

Since the relative RMSE is an aggregated metric, the spread of errors is evaluated by taking the 2 % and 98 % percentiles of the relative absolute

errors,

$$Q_p \left(\max_{i=1, \dots, N_x} \frac{|\mathbf{x}_i - \hat{\mathbf{x}}_i|}{\max_{k \in 1, \dots, N_T} x_{k,i} - \min_{k \in 1, \dots, N_T} x_{k,i}} \right). \quad (12)$$

Hence, the spread is expressing the temporal extremes of the absolute errors relative to the spatial variability. Using the maximum as an aggregator across space ensures that extreme values are represented.

At observation stations, we compare both MIKE 21 and surrogate predictions against measurements and report the percentage increase in RMSE when using the surrogate. A surrogate meeting an objective of 90% skill retention would have RMSE increase $< 10\%$ relative to the physics-based model. This framing recognizes that surrogate accuracy is bounded by the physics model's own structural errors; the goal is to preserve predictive skill rather than match simulation outputs exactly.

3.3. Fairness and practical interpretation of model comparisons

All surrogate model architectures are compared for the same test case using a fixed latent space dimensionality and are trained and evaluated on identical computational hardware. This ensures fair comparisons of accuracy, training time, and inference time across architectures. The physics-based ocean model used for data generation is run on a different machine and employs a different time-stepping scheme. Consequently, timing comparisons between the physics-based model and the surrogate models are not intended as controlled hardware benchmarks, but rather as a practical comparison reflecting typical execution environments: high-fidelity ocean simulations on specialized computing resources versus surrogate models trained and deployed on readily available machine-learning hardware.

4. Results

4.1. Latent space dimension

The latent space dimension and the autoencoder composition cf. Figure 2 is determined by analysis of reconstruction-prediction error trade-offs observed. Increasing dimension improves reconstruction, but it does not necessarily improve prediction. This trade-off is assessed qualitatively using the PODLR surrogate for deciding the latent space dimensions. An overview of the chosen dimensions is found in Appendix B.1.

The best reconstruction is achieved with a concatenated state autoencoder structure for Øresund, and a separated autoencoder for Adriatic Sea and Southern North Sea. The reason is evident in Figure 5, which shows the reconstruction errors of the state variables in the Adriatic Sea case with a concatenated POD on the left and a separated POD autoencoder on the right, where U and V are separated from S . In the concatenated POD, the reconstruction error of S follows that of U and V , while in the separated POD, the reconstruction of S is very accurate even for few modes. Based on this specific figure, it is decided to use 10 modes for S and 50 modes for (U, V) , yielding reconstruction errors of around $4 \cdot 10^{-3}$ and $7 \cdot 10^{-3}$ for the two groups, respectively. In comparison, a concatenated POD with latent dimension of 60 would yield errors around $7 \cdot 10^{-3}$ for all variables. Similar conclusions are drawn for the reconstruction errors of the forcings, where the autoencoder is concatenated in the Øresund case, and the BCs and wind-related forcings are separated in Adriatic and Southern North Sea.

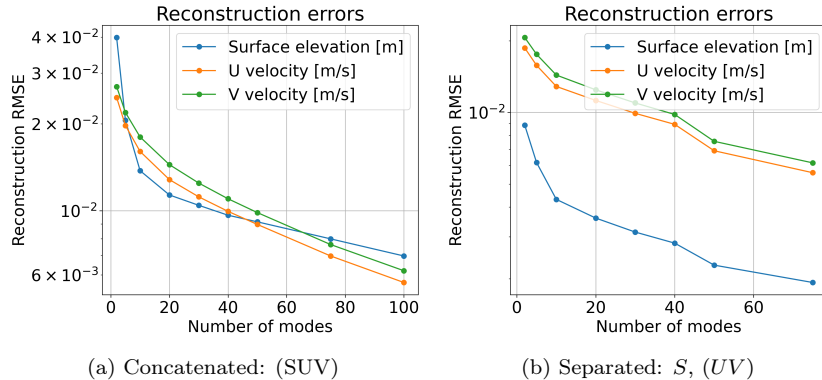


Figure 5: Reconstruction RMSEs for POD in the Adriatic test case.

For analyzing the effect on latent space dimension on the prediction error, Figure 6 shows the prediction RMSE in a validation period for the Øresund test case for different dimensions of the state and forcing latent spaces. The leftmost figure shows the PODLR model, and the rightmost is the PODLRT (TU) model. While the reconstruction errors monotonically decreases with increasing dimension, the prediction errors actually explode in the PODLR. The reason is that the linear regression is unstable for the increasing number of input variables. Applying temporal unrolling solves the instability issues, but the same pattern is evident here: there is an optimal number of latent

dimensions, which is not simply the largest possible, but somewhere around 20 for the state and 50 for the forcings.

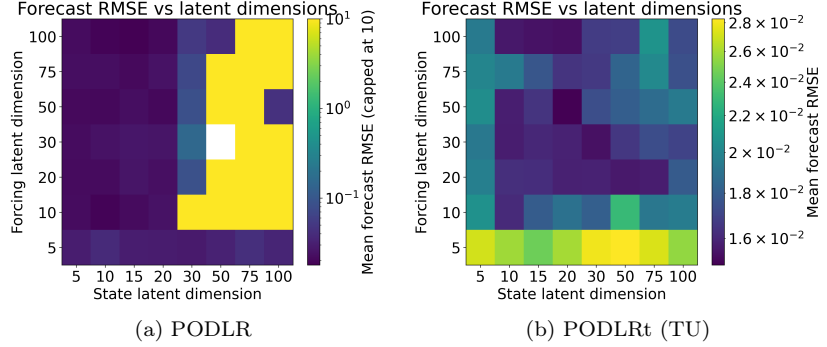


Figure 6: Prediction RMSE in a validation period for the Øresund case.

4.2. Surrogate prediction performance

Figure 7 shows an example of a surface elevation prediction made for the Southern North Sea with the LKAE (TU) model. The prediction is based on auto-regressive temporal steps and the shown time-step corresponds to the median prediction RMSE, hence, the figures reflect the median performance. Generally, the LKAE estimates the MIKE 21 simulation output very well, with the largest errors located close to the coast in the South and in the East.

Figure 8 shows the relative prediction RMSE together with 2 and 95 % percentiles for the different surrogate models based on an autoregressive prediction of the surface elevations in the test period of the three cases.

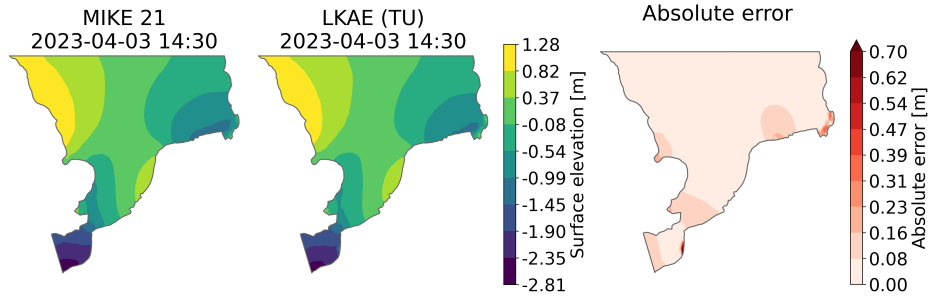


Figure 7: Prediction of surface elevations with the MIKE 21 and the LKAE (TU) in the time-step corresponding to median RMSE.

The conclusions based on the surface elevations are representative also for the prediction of currents, but for completeness, the figures for the u - and v -component of the current velocities are found in Appendix C.1. Figure 9 shows the wall-clock time spent per epoch when training the surrogate model for the Øresund case. The patterns are similar in the other two cases.

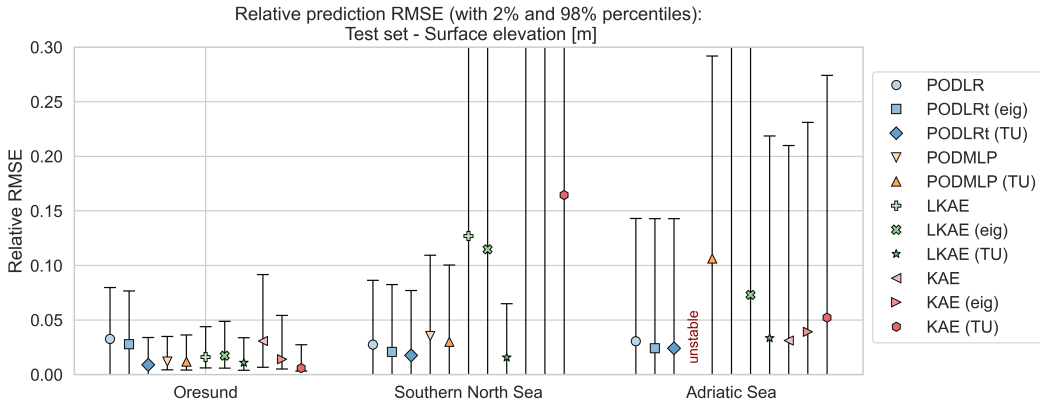


Figure 8: Test RMSE relative to the range of values of the surface elevation. The bars represent the 2% and 98% percentiles according to (12).

In one case, the surrogate is found to be unstable for autoregressive roll-outs, namely the PODMLP for Adriatic Sea. Using eigenvalue regularization stabilizes the surrogate to an acceptable level (relative RMSE ≈ 0.1). The eigenvalue regularization is also effective for improving accuracy of the PODLRt model for all cases, and of the KAE for Øresund and LKAE for Adriatic Sea.

Across all cases and model architectures, except the nonlinear KAE for Adriatic Sea, temporal unrolling has a positive effect on the accuracy and/or stability of the surrogate. For instance, using temporal unrolling for the PODLRt improves the accuracy in all cases. Most remarkable is the effect on the KAE for Øresund, where the relative RMSE reduces to 0.01 when using temporal unrolling, as well as the LKAE for Southern North Sea, where the relative RMSE reduces from 0.13 to 0.016.

The computational complexity analysis in Section 2.5 explains the training-time differences observed in Figure 9 and reveals a clear offline–online trade-off. POD-based surrogates offer very low offline cost, while Koopman autoencoders require higher training effort but deliver improved stability and long-horizon accuracy. The figure even shows that the temporal unrolling

implementation for the POD-based models is more effective than the regular implementation, which can be explained by a more efficient batch implementation. Further, as expected from the computational complexity, the effect of applying eigenvalue regularization is minor. Since online inference time-complexities are comparable across surrogate classes, model choice is primarily governed by available training resources and required robustness in deployment.

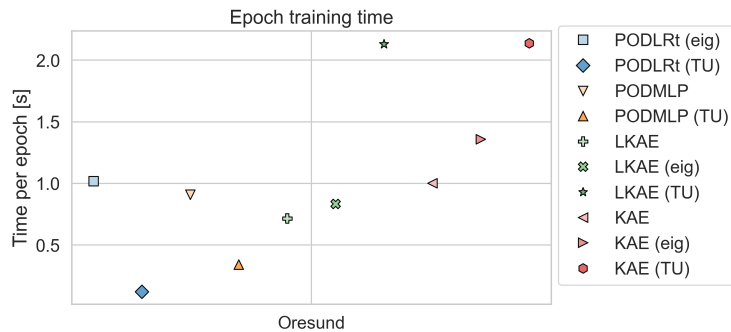


Figure 9: Time spent per epoch when training models. Total time for each model, in the order of the plot: 124, 21.5, 369, 63.7, 185, 204, 831, 454, 500, 1550 seconds. PODLR takes 10 seconds (not shown in plot).

4.3. Analysis of best surrogates

The best-performing model in terms of accuracy is the KAE (TU) for Øresund, and LKAE (TU) for Southern North and Adriatic Seas, and their R^2 -performance in the test-period is shown in Table 2. For Øresund, the 95%-percentile of the relative errors is below 0.05 across state variables, and the R^2 are very close to 1. For Southern North Sea, the 95%-percentile is below 0.1 across states, and the R^2 are also very high. For the Adriatic Sea, however, the 95%-percentile relative errors range up to 0.3, and the R^2 is further from 1, especially for the current velocity components (U, V), suggesting that the ocean dynamics in the Adriatic Sea are more difficult to represent with the proposed architectures.

Complementary to the aggregated metrics, the RMSE can be computed for each spatial element, as visualized in Figure 10 and the figures in Appendix C.3. The plots show the errors for the autoregressive predictions across the test periods. In Øresund, the largest errors are in the North, yet they are only on the scale of a few centimeters. In the Southern North Sea,

Table 2: R^2 values in the test-period. The closer R^2 is to 1, the better.

	Øresund KAE (TU)	S. North Sea LKAE (TU)	Adr. Sea LKAE (TU)
S	0.996	0.993	0.940
R^2	0.993	0.986	0.732
V	0.995	0.986	0.650

the largest errors range up to around 20 cm, and they are located close to the Eastern part of the domain, which is the Wadden Sea off the West-coast of Denmark and Northern Germany. This area is known for its very shallow waters, and the especially the low water levels are not as well captured by the surrogate as the deeper waters. In the Adriatic Sea, the largest errors are located in the Northwestern end of the basin, as expected due to the seiching occurring in this area. Yet, the RMSEs are relatively small, ranging up to 8.5 cm, indicating that on average the surface elevation predictions are very accurate.

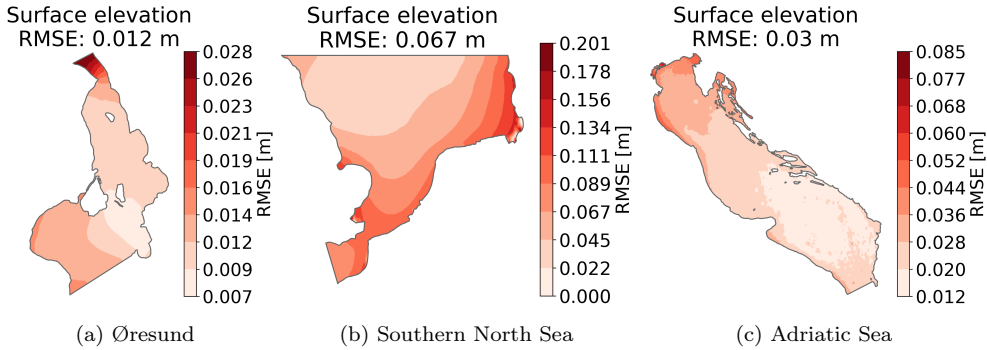


Figure 10: RMSE across time for each test case

Figure 11 shows scatter plots of the predicted S values on the y -axis compared to the MIKE 21 values on the x -axis. The values are shown only for a location corresponding to a measurement station for each test case. Similar figures for the other two state variables are found in Appendix C.2. The leftmost figure shows that the surrogate for Øresund predicts the MIKE 21 data to a very satisfying extent with the dots close to the diagonal line, also for extreme values. For Southern North Sea, there is some tendency for the surrogate to underestimate the large surface elevations and overestimate the low elevations as discussed for the Wadden Sea.

The right-most scatter plot once again showcases that the surrogate is not capturing the simulation data for Adriatic Sea to the same extent as for the other two cases. One explanation is the complex resonant oscillations in the basin, especially close to Venice where the ISMAR-CNR platform is located. Compared to the two other test-cases, there is fewer data available for training the surrogate, and the results indicate that more training and more data could be beneficial.

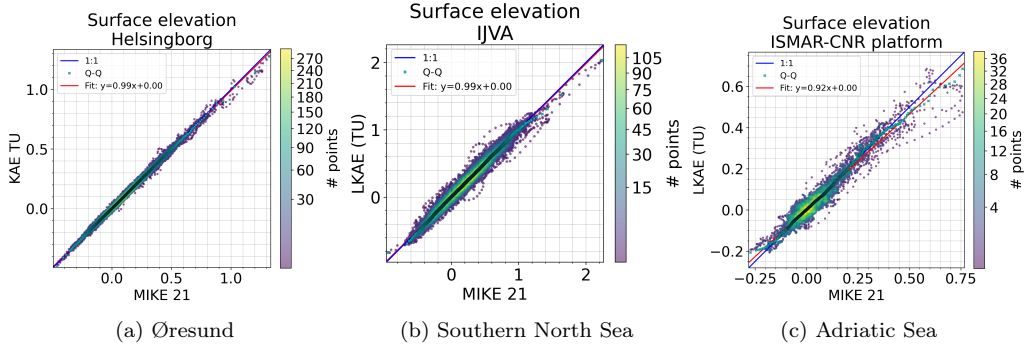


Figure 11: Scatter plots of the simulation data (x-axis) vs. the surrogate predictions (y-axis) in the test period for a single spatial point. Surface elevations.

4.4. Comparing surrogate performance with MIKE 21

Since the surrogate model performance is, in principle, bounded by the physics-based model's prediction skill, the aim of the surrogate is to preserve skill. To assess the preservation level, Table 3 shows the RMSEs of the physics-based MIKE 21 model and of the best performing surrogate when validating the predictions against observations. The bottom row indicates the percentage increase in RMSE when using the surrogate compared to MIKE 21, and a low percentage means successful retention of skill. It is confirmed that the Koopman based surrogate would be an excellent choice for emulating Øresund. For Southern North Sea and Adriatic Sea, the performance is also satisfactory. Yet, at the IJVA station, there is an error increase of 12%, but when the MIKE 21 model yields a prediction RMSE of 14.7 cm, and the LKAE (TU) surrogate produces an RMSE of 16.4 cm, this marginal increase could be acceptable for practical applications.

Combining this result with the time spent on inference in a one-year simulation seen in Table 4, there is a clear advantage of using the surrogate,

Table 3: RMSEs and the relative increase in RMSE of the models in the test period compared to observations in measurement stations. RMSEs given in centimeters. Surrogate models are KAE (TU), LKAE (TU) and LKAE (TU) for the three cases, respectively. Hels.: Helsingborg, Kbh.: København, Dro.: Drogden.

RMSE	Øresund			S. North Sea			Adr. Sea
	Hels.	Kbh.	Dro.	IJVA	F3	J61	ISMAR-CNR
MIKE 21 [cm]	7.24	5.77	6.27	14.7	12.3	16.4	5.68
Surrogate [cm]	7.28	5.80	6.23	16.4	13.2	17.5	6.00
Increase [%]	0.51	0.44	-0.64	12	7.3	6.7	5.6

namely that a factor 300-1400 speed-up is achieved. This speed-up is calculated under the conditions that the physics-based simulation is performed on a GPU, which is normal practice in industry, whereas the surrogate is simply run on a laptop CPU. However, the potential application of the surrogate exceeds the one-year simulation: with such a fast surrogate, one could perform hundreds of simulations, e.g. for ensembles for uncertainty quantification, or one could perform very long simulations, which is otherwise not feasible with the physics-based model.

Table 4: Simulation time for a 1 year simulation for the three test cases. Excluding training times for surrogates or calibration times for physics-based model. Surrogate models are KAE (TU), LKAE (TU) and LKAE (TU) for the three cases, respectively. Machine used: MIKE 21 Øresund, S. North Sea: NVIDIA A40 GPU, MIKE 21 Adriatic Sea: Nvidia Quadro M2000, surrogates: Laptop CPU (13th Gen Intel(R) Core(TM) i7-1365U with 32 GB RAM.)

Inference time	Øresund	S. North Sea	Adriatic
MIKE 21 [s]	2600	1200	16800
Surrogate [s]	4	4	12
Speed-up factor	650	300	1400

5. Discussion

This paper has investigated reduced-order surrogate models for physics-based numerical models solving the shallow-water equation. The main assumption behind the work is that the dynamics of the system variables observed on the flexible mesh can be reduced to a limited number of dominant modes. Without this property, e.g. revealed by slow decay of the singular

values when using POD, the reduced-order model cannot sufficiently resolve the data. The analysis of reconstruction errors in this work showed that the data can be resolved to a sufficient level given relatively few modes: 10-50 modes for mesh data with thousands of elements. However, there is an important trade-off when compressing data: while high simulation speed is achieved, some accuracy is lost. In the Southern North Sea case, this was evident with RMSE increases up to 12%, when using the surrogate instead of the original numerical model. However, for most practical applications, the increase in absolute numbers (on the order of a few centimeters) is generally acceptable given the factor 300-1400 speed-up. While the reported speed-ups are intended to reflect realistic operational usage rather than controlled hardware benchmarks, they work as an indicator of the potential gains from using the reduced order surrogates.

Two types of surrogates were tested for forced coastal-ocean systems, namely POD and KAEs, as well as two types of strategies for improving long-term prediction stability and accuracy. The key distinction lies in how each method handles the latent space: POD provides an optimal linear basis for reconstruction but makes no assumptions about temporal dynamics, whereas KAE promotes linear dynamics through end-to-end training of the autoencoder and propagator. This is evident across all test cases, where the linear KAE, which has the same number of parameters as the PODLR, achieves better accuracies with relative RMSEs of 0.01–0.13. Further, the KAEs yield stable long-term predictions with learned Koopman operator eigenvalues within the unit circle, even in the cases where the errors are large. In other words, the end-to-end training ensures a meaningful latent space with stable dynamics.

However, there is a caveat when using the KAE architecture: while the autoencoder is flexible and can achieve high accuracy, it is obtained through non-convex optimization of parameters. The POD, on the other hand, ensures an optimal low-rank reconstruction via the singular value decomposition. An alternative, which ensures an optimal latent linear evolution operator, is the dynamic mode decomposition (DMD), which determines the best-fit linear operator, yielding modes and eigenvalues that optimally capture the observed dynamics (Schmid, 2010; H. Tu et al., 2014). While there exist extensions of the DMD appropriate for the current study, e.g. DMD with control (Proctor et al., 2014), this approach remains a direction for future work, since interest of the current study was in exploring the flexibility of using neural network architectures for the KAE e.g. for eigenvalue

regularization, temporal unrolling and separation of autoencoders.

By construction, the surrogate models are trained to perform well on average given the MSE-based loss function. While the current work includes some extreme value analysis, future work will explore whether performance can be improved for extreme value predictions for applications e.g. in early warning systems. In addition, generalization to unseen or out-of-distribution forcing conditions, could be investigated more thoroughly in future work. Another potential direction is exploring emulator superiority over the physics-based simulation used for generating training data. For instance, using the surrogate for data assimilation, thereby ensuring closer resemblance to observed values, or by exploring to what extent the surrogate can outperform the physics-based model e.g. by implicit regularization that may reduce numerical artifacts (Koehler and Thuerey, 2025).

6. Conclusion

The proposed Koopman autoencoder (KAE) architecture with external forcing inputs and temporal unrolling was superior to proper orthogonal decomposition (POD) based surrogates in terms of accuracy across three hydrodynamic test cases. The proposed eigenvalue regularization effectively improved long-term stability in unstable surrogates, but did not yield the same accuracy improvements as temporal unrolling. For most surrogates, temporal unrolling improved the accuracy by a factor two. The best-performing surrogate models were KAEs, which achieved RMSEs in the range 0.01–0.13 relative to the variability of the predicted variables in autoregressive predictions of one year with 30 minute time steps. The R^2 values were 0.940–0.996 for water surface elevations and 0.65–0.996 for current velocities. The highest errors were observed for one test case which has limited training data, a large mesh and complicated dynamics due to seiching.

When surrogate model prediction skill was compared to the physics-based hydrodynamic model skill when validated against in-situ observations, the RMSE increased by at most 12%, corresponding to errors of a few centimeters. In one case, errors decreased due to an improved prediction skill with the surrogate. Together with inference-time speed-ups of 300 to 1400 times for one-year simulations, these results indicate that the proposed reduced-order KAE surrogates are well suited for practical applications in ocean modelling.

Acknowledgements

This work was funded in part by Innovation Fund Denmark, project no. 4297-00048B and in part by DHI's research contract with the Danish Ministry of Higher Education and Science. The operational model setup for the Adriatic Sea is funded by Ministero delle Infrastrutture e dei Trasporti, Provveditorato Interregionale alle OO. PP. del Veneto, Trentino Alto Adige, Friuli Venezia Giulia.

Data and code availability

Two of the three datasets used in this study are publicly available via a persistent repository (Zenodo). The third dataset is subject to third-party and/or operational constraints and cannot be shared publicly.

The research code used to develop and train the surrogate models is not publicly available at this stage due to intellectual property considerations and ongoing work towards potential commercialization. The paper provides a complete description of the methods, model formulations, and experimental setup to allow independent reproduction of the approach.

Declaration of generative AI use

During the preparation of this work the author(s) made limited use of ChatGPT and the use was restricted to improving language and flow of the text, and not for any conceptual work. After using this tool/service, the author(s) reviewed and edited the content as needed and take(s) full responsibility for the content of the published article.

References

Akiba, T., Sano, S., Yanase, T., Ohta, T., Koyama, M., 2019. Optuna: A next-generation hyperparameter optimization framework, in: Proceedings of the 25th ACM SIGKDD International Conference on Knowledge Discovery and Data Mining.

Azencot, O., Erichson, N.B., Lin, V., Mahoney, M.W., 2020. Forecasting Sequential Data using Consistent Koopman Autoencoders. doi:10.48550/arXiv.2003.02236.

Bogaard, T., de Lima Rego, J., Vatvani, D., Virasami, R., Verlaan, M., 2016. The early-warning system for incoming storm surge and tide in the republic of mauritius, in: EGU General Assembly, Geophysical Research Abstracts.

Brettin, A.E., Zanna, L., Barnes, E.A., 2025. Learning Propagators for Sea Surface Height Forecasts Using Koopman Autoencoders. Geophysical Research Letters 52. doi:10.1029/2024GL112835.

Brunton, S.L., Brunton, B.W., Proctor, J.L., Kutz, J.N., 2016. Koopman invariant subspaces and finite linear representations of nonlinear dynamical systems for control. PLoS ONE 11. doi:10.1371/journal.pone.0150171.

Città di Venezia, 2025. 3. piattaforma ismar-cnr. URL: <https://comune.venezia.it/it/content/3-piattaforma-ismar-cnr>. visited: 2025-12-15.

CMEMS, 2024a. E.U. Copernicus Marine Service Information (CMEMS). In-situ ocean TAC. URL: <https://marineinsitu.eu/dashboard/>. visited: 2024-11-11.

CMEMS, 2024b. E.U. Copernicus Marine Service Information (CMEMS). Marine Data Store (MDS): Baltic Sea- In Situ Near Real Time Observations. doi:10.48670/moi-00032. visited: 2024-10-02.

Deo, M., Sridhar Naidu, C., 1998. Real time wave forecasting using neural networks. Ocean Engineering 26, 191–203. doi:10.1016/S0029-8018(97)10025-7.

DHI, 2023. IJmuiden ver wind farm zone. part a: Metocean modelling. URL: https://offshorewind.rvo.nl/file/download/bfa49f34-f894-4562-882f-eb1a8b7497e9/ijv_20231222-dhi-metocean-modelling.pdf.

DHI, 2024a. Hydrodynamic model of Øresund: MIKE 21 model setup, outputs and observation data. doi:10.5281/zenodo.14160710. (1.0) [Dataset].

DHI, 2024b. MIKE 21 Flow Model FM - Hydrodynamic Module and Transport module - Scientific Documentation. DHI A/S. URL: https://manuals.mikepoweredbydhi.help/latest/Coast_and_Sea/MIKE_21_Flow_FM_Scientific_Doc.pdf. (visited: 2025-12-18).

DHI, 2024c. Protecting Venice from high water levels. URL: <https://www.dhigroup.com/projects/protecting-venice-from-high-water-levels>. (visited: 2025-12-30).

DHI, 2025. Hydrodynamic model of the Southern North Sea: MIKE 21 model setup, outputs and observation data. doi:10.5281/zenodo.14929387. (1.0) [Dataset].

H. Tu, J., W. Rowley, C., M. Luchtenburg, D., L. Brunton, S., Nathan Kutz, J., 2014. On dynamic mode decomposition: Theory and applications. *Journal of Computational Dynamics* 1, 391–421. doi:10.3934/jcd.2014.1.391.

Halko, N., Martinsson, P.G., Tropp, J.A., 2010. Finding structure with randomness: Probabilistic algorithms for constructing approximate matrix decompositions. [arXiv:0909.4061](https://arxiv.org/abs/0909.4061).

Herzen, J., Lässig, F., Piazzetta, S.G., Neuer, T., Tafti, L., Raille, G., Pottelbergh, T.V., Pasieka, M., Skrodzki, A., Huguenin, N., Dumonal, M., Koscisz, J., Bader, D., Gusset, F., Benheddi, M., Williamson, C., Kosinski, M., Petrik, M., Grosch, G., 2021. Darts: User-friendly modern machine learning for time series. *CoRR* abs/2110.03224. [arXiv:2110.03224](https://arxiv.org/abs/2110.03224).

Jiang, P., Meinert, N., Jordão, H., Weisser, C., Holgate, S., Lavin, A., Lütjens, B., Newman, D., Wainwright, H., Walker, C., Barnard, P., 2021. Digital twin earth – coasts: Developing a fast and physics-informed surrogate model for coastal floods via neural operators. [arXiv:2110.07100](https://arxiv.org/abs/2110.07100).

Kaiser, E., Kutz, J.N., Brunton, S.L., 2021. Data-driven discovery of Koopman eigenfunctions for control. *Machine Learning: Science and Technology* 2, 035023. doi:10.1088/2632-2153/abf0f5.

Kingma, D.P., Ba, J., 2017. Adam: A method for stochastic optimization.

Koehler, F., Thuerey, N., 2025. Neural emulator superiority: When machine learning for PDEs surpasses its training data. [arXiv:2510.23111](https://arxiv.org/abs/2510.23111).

Koopman, B.O., 1931. Hamiltonian systems and transformation in Hilbert space. *Proceedings of the National Academy of Sciences* 17, 315–318. doi:10.1073/pnas.17.5.315.

Lesser, G.R., Roelvink, D.A., van Kester, J.A.T.M., Stelling, G.S., 2004. Development and validation of a three-dimensional morphological model. *Coastal Engineering* 51, 883–915. doi:10.1016/j.coastaleng.2004.07.014.

Lightning AI, 2025. The ai cloud pytorch developers love. URL: <https://lightning.ai/>. visited: 2025-12-17.

List, B., Chen, L.W., Bali, K., Thuerey, N., 2024. Differentiability in unrolled training of neural physics simulators on transient dynamics. [arXiv:2402.12971](https://arxiv.org/abs/2402.12971).

Lortie, L., Dahdah, S., Forbes, J.R., 2024. Forward-Backward Extended DMD with an Asymptotic Stability Constraint. [arXiv:2403.10623](https://arxiv.org/abs/2403.10623).

Loshchilov, I., Hutter, F., 2017. Fixing weight decay regularization in Adam. *CoRR* abs/1711.05101. [arXiv:1711.05101](https://arxiv.org/abs/1711.05101).

Luettich, R.A., Westerink, J.J., Scheffner, N.W., 1992. ADCIRC: An advanced three-dimensional circulation model for shelves, coasts, and estuaries. Report 1: Theory and methodology. Technical Report DRP-92-6. U.S. Army Engineer Waterways Experiment Station. Vicksburg, Mississippi.

Mezić, I., 2005. Spectral Properties of Dynamical Systems, Model Reduction and Decompositions. *Nonlinear Dynamics* 41, 309–325. doi:10.1007/s11071-005-2824-x.

Morton, J., Witherden, F.D., Kochenderfer, M.J., 2019. Deep variational Koopman models: Inferring Koopman observations for uncertainty-aware dynamics modeling and control. [arXiv:1902.09742](https://arxiv.org/abs/1902.09742).

Nayak, I., Chakrabarti, A., Kumar, M., Teixeira, F.L., Goswami, D., 2025. Temporally-consistent Koopman autoencoders for forecasting dynamical systems. *Scientific Reports* 15, 22127. doi:10.1038/s41598-025-05222-7.

NEA, 2024. Netherlands Enterprise Agency: IJmuiden Ver - Wind & Water.
URL: <https://offshorewind.rvo.nl/page/view/4c4cb8e3-a1c7-404f-917f-a2f6e0d8c803/wind-en-water-ijmuiden-ver>. visited: 2024-11-08.

Nogueira, A.C., Almeida, J.L.d.S., Auger, G., Watson, C.D., 2020. Reduced Order Modeling of Dynamical Systems Using Artificial Neural Networks Applied to Water Circulation. Springer International Publishing. p. 116–136. doi:10.1007/978-3-030-59851-8_8.

Otto, S.E., Rowley, C.W., 2019. Linearly-recurrent autoencoder networks for learning dynamics [arXiv:1712.01378](https://arxiv.org/abs/1712.01378).

Paszke, A., Gross, S., Massa, F., Lerer, A., Bradbury, J., Chanan, G., Killeen, T., Lin, Z., Gimelshein, N., Antiga, L., Desmaison, A., Köpf, A., Yang, E., DeVito, Z., Raison, M., Tejani, A., Chilamkurthy, S., Steiner, B., Fang, L., Bai, J., Chintala, S., 2019. Pytorch: An imperative style, high-performance deep learning library. [arXiv:1912.01703](https://arxiv.org/abs/1912.01703).

Pedregosa, F., Varoquaux, G., Gramfort, A., Michel, V., Thirion, B., Grisel, O., Blondel, M., Prettenhofer, P., Weiss, R., Dubourg, V., Vanderplas, J., Passos, A., Cournapeau, D., Brucher, M., Perrot, M., Duchesnay, E., 2011. Scikit-learn: Machine learning in Python. *Journal of Machine Learning Research* 12, 2825–2830.

Proctor, J.L., Brunton, S.L., Kutz, J.N., 2014. Dynamic mode decomposition with control. [arXiv:1409.6358](https://arxiv.org/abs/1409.6358).

Proctor, J.L., Brunton, S.L., Kutz, J.N., 2018. Generalizing Koopman Theory to Allow for Inputs and Control. *SIAM Journal on Applied Dynamical Systems* 17, 909–930. doi:10.1137/16M1062296.

Pytorch, 2025a. Adamw. URL: <https://docs.pytorch.org/docs/stable/generated/torch.optim.AdamW.html>. urldate: 2025-12-19.

Pytorch, 2025b. ReduceLROnPlateau. URL: https://docs.pytorch.org/docs/stable/generated/torch.optim.lr_scheduler.ReduceLROnPlateau.html. visited: 2025-12-22.

Rice, J., Xu, W., August, A., 2021. Analyzing Koopman approaches to physics-informed machine learning for long-term sea-surface temperature forecasting. [arXiv:2010.00399](https://arxiv.org/abs/2010.00399).

Rivera-Casillas, P., Dutta, S., Cai, S., Loveland, M., Nath, K., Shukla, K., Trahan, C., Lee, J., Farthing, M., Dawson, C., 2025. A Neural Operator-Based Emulator for Regional Shallow Water Dynamics. doi:10.48550/arXiv.2502.14782.

Schmid, P.J., 2010. Dynamic mode decomposition of numerical and experimental data. *Journal of Fluid Mechanics* 656, 5–28. doi:10.1017/S0022112010001217.

Shi, H., Meng, M.Q.H., 2022. Deep Koopman Operator with Control for Nonlinear Systems. doi:10.48550/arXiv.2202.08004.

Vieira, J., Føns, J., Cecconi, G., 1993. Statistical and hydrodynamic models for the operational forecasting of floods in the venice lagoon. *Coastal Engineering* 21, 301–331. doi:10.1016/0378-3839(93)90012-W.

Appendix A. Test cases

This section presents information relevant to the three test cases.

Appendix A.1. Forcing variables and dimensions

Table A.5 gives an overview of the forcing variables and their dimensions in each case. In all cases, the boundary conditions are given as all three state variables, S , U , and V , therefore there is a factor 3 on the dimension. The wind and air pressure are given on 2D grids, and consist of a total of three variables as well (u- and v-component of wind velocities, air pressure). In the Adriatic Sea case, the wind and air pressure grid has been reduced by removing all grid cells that correspond to over-land values, such that only over-sea values are included. Therefore only 1448 out of the 4200 grid cells are active. The total number of forcing dimensions, N_u , is given in the first column.

The forcing data for the Øresund and Southern North Sea data is publicly available together with the MIKE 21 model setups and the simulation data used for this paper (DHI, 2024a, 2025).

Table A.5: Overview of forcing variables in the three test cases.

Case	Forcing	Dimension
\mathcal{O} resund $N_u = 168$	North BC	$3 \cdot 13$
	South BC	$3 \cdot 27$
	Wind and Air pressure	$3 \cdot (4 \cdot 4)$
Southern North Sea $N_u = 7275$	North BC	$3 \cdot 16$
	South BC	$3 \cdot 9$
	Wind and Air pressure	$3 \cdot (48 \cdot 50)$
Adriatic Sea $N_u = 4404$	BC	$3 \cdot 20$
	Wind and Air pressure	$3 \cdot (75 \cdot 56)$ (only $3 \cdot 1448$ active)

Appendix A.2. Observation stations

Observations from in-situ measurement stations are used for comparison to the MIKE 21 and surrogate predictions. The stations together with their coordinates and the sources of the data are listed in Table A.6.

Table A.6: Overview of measurement stations used for validating the surrogate model. Coordinates (longitude/latitude) and reference to the source.

Case	Station	Longitude	Latitude	Source
Øresund	Helsingborg	12.6845	56.0412	DHI (2024a) /
	København	12.65	55.7	CMEMS (2024b)
	Drogden	12.7117	55.5358	
Southern North Sea	IJVA	3.71044	52.88381	DHI (2025) /
	F3 platform	4.72000	54.84999	NEA (2024) /
	J61	2.94380	53.82325	CMEMS (2024a)
Adriatic Sea	ISMAR- CNR	12.51472	45.32306	Città di Venezia (2025)

Appendix B. Parameters

This section provides an insight into the parameters of the surrogate models. Specifically the number of latent dimensions used in each test case, as well as all hyper-parameters used for the surrogate models. For the analyses and hyper-parameter tuning a subset of the training data is used for training and validation. The periods are shown in Table B.7.

Table B.7: Training and validation periods for hyper-parameter tuning

	Øresund	S, North Sea	Adriatic Sea
Train period	Jan-Apr 2021	Jan-Feb 2022	Jan-Feb 10 2021
Val. period	May-Jun 2021	Mar 2022	Feb 11-Feb 28 2021

Appendix B.1. Latent dimensions and reconstruction errors

Across surrogate models the same number of latent dimensions is used regardless of whether it is Koopman-based, POD-based, concatenated or separated autoencoders. Table B.8 shows an overview of the dimensions and reconstruction errors for each type of model. If only one latent dimension is given, it means that the autoencoder is concatenated. E.g. for Southern North Sea the U and V variables are concatenated in one autoencoder with latent dimension 20. The latent dimensions are chosen based on an analysis as described in Section 4.1.

The RMSE Koopman column corresponds to the reconstruction of the states with the best performing Koopman-based surrogate. The last columns

shows the value range (mean across spatial elements) for each variable. Table B.9 shows corresponding results for the forcing variables. However, since the forcings are only encoded and not decoded in the Koopman surrogates, it is only the POD reconstruction, which is shown.

Table B.8: Number of modes and the resulting reconstruction errors for each state variable in the three test cases. Evaluated on the training period. S : Surface elevation, U : U-component of velocity, V : V-component of velocity. For Øresund, the Koopman model is the KAE (TU), for S. North Sea and Adriatic Sea it is LKAE (TU).

Case	State	Latent dim.	RMSE POD	RMSE Koopman	Unit	Value range
Øresund	S	15	$5.8 \cdot 10^{-3}$	$3.2 \cdot 10^{-3}$	m	1.4
	U		$4.6 \cdot 10^{-3}$	$3.0 \cdot 10^{-3}$	m/s	0.32
	V		$6.5 \cdot 10^{-3}$	$4.5 \cdot 10^{-3}$	m/s	0.63
S. North Sea	S	20	$1.7 \cdot 10^{-2}$	$2.7 \cdot 10^{-2}$	m	3.9
	U	20	$1.8 \cdot 10^{-2}$	$1.1 \cdot 10^{-2}$	m/s	1.0
	V		$1.6 \cdot 10^{-2}$	$1.1 \cdot 10^{-2}$	m/s	0.98
Adriatic Sea	S	10	$6.2 \cdot 10^{-3}$	$1.5 \cdot 10^{-2}$	m	0.84
	U	50	$9.1 \cdot 10^{-3}$	$1.1 \cdot 10^{-2}$	m/s	0.21
	V		$1.0 \cdot 10^{-2}$	$1.2 \cdot 10^{-2}$	m/s	0.22

Table B.9: Number of components and the resulting reconstruction errors for each forcing in the three test cases.

Case	Forcing	Latent dim.	RMSE POD	Unit	Value range
Øresund	North BC S	50	$1.3 \cdot 10^{-3}$	m	1.4
	North BC U		$1.9 \cdot 10^{-3}$	m/s	1.2
	North BC V		$1.8 \cdot 10^{-3}$	m/s	0.90
	South BC S		$1.5 \cdot 10^{-3}$	m	1.6
	South BC U		$4.0 \cdot 10^{-4}$	m/s	0.22
	South BC V		$1.6 \cdot 10^{-3}$	m/s	0.96
	Air pressure		$1.1 \cdot 10^{-1}$	hPa	69
	Wind U		$5.2 \cdot 10^{-2}$	m/s	22
	Wind V		$4.5 \cdot 10^{-2}$	m/s	22
S. North Sea	North BC S	10	$3.9 \cdot 10^{-2}$	m	2.9
	North BC U		$1.2 \cdot 10^{-2}$	m/s	0.62
	North BC V		$1.8 \cdot 10^{-2}$	m/s	0.84
	South BC S	10	$8.0 \cdot 10^{-3}$	m	7.4
	South BC U		$4.7 \cdot 10^{-3}$	m/s	2.2
	South BC V		$1.9 \cdot 10^{-3}$	m/s	1.0
	Wind U	10	1.4	m/s	32
	Wind V		1.3	m/s	28
	Air pressure		0.64	hPa	69
Adriatic Sea	BC S	10	$1.6 \cdot 10^{-3}$	m	0.56
	BC U		$1.0 \cdot 10^{-3}$	m/s	0.065
	BC V		$3.3 \cdot 10^{-3}$	m/s	0.21
	Air pressure	60	0.26	hPa	43.7
	Wind U		0.80	m/s	25
	Wind V		0.84	m/s	28

Appendix B.2. Hyper-parameters

A number of hyper-parameters are used when fitting the surrogate models. An overview of the hyper-parameters used in each test case is given in tables B.10 (Øresund), B.12 (Adriatic Sea), and B.11 (Southern North Sea). For the POD-based models, the hyper-parameters only concerns the temporal propagator in the latent space, since the POD itself is computed using a closed form solution. Since the PODMLP is not linear in the latent space, an eigenvalue regularized version does not exist and the middle row is therefore

irrelevant.

All models are trained with a learning rate scheduler which is the PyTorch `ReduceLROnPlateau` (Pytorch, 2025b). Unless otherwise specified in the tables, the methods use the default variables, e.g. momentum variables for the Adam optimizers.

The TU steps and TU window stride are two important parameters in the implementation of temporal unrolling. The temporal unrolling is implemented in a batch-parallelized manner such that within one batch, different unrollings of length 'TU steps' are initiated at the same time with 'TU window stride' space. E.g. if 'TU window stride' is 1, the unrolled sequences would be

$$\begin{aligned} \text{Thread 1: } & x_1, x_2, \dots, x_{\text{TU steps}} \\ \text{Thread 2: } & x_2, x_3, \dots, x_{\text{TU steps}+1} \\ & \vdots \end{aligned}$$

If 'TU window stride' is w , the sequences would be:

$$\begin{aligned} \text{Thread 1: } & x_1, x_2, \dots, x_{\text{TU steps}} \\ \text{Thread 2: } & x_{1+w}, x_{2+w}, \dots, x_{\text{TU steps}+w} \\ & \vdots \end{aligned}$$

Hence, the parameter 'TU steps' needs to be smaller than the batch size.

In the following sections, the hyper parameters will be presented. A few common abbreviations are used to compress the table: Optim.=Optimizer, LR=Learning rate, W.D.=weight decay, LR sche.=Learning rate scheduler, pat.=patience, fac.=factor, tol.=tolerance, TU win.=temporal unrolling window. Note that all autoencoders are symmetric, meaning that there are the same number of parameters (layers and hidden dimensions) in the encoder and decoder.

Appendix B.2.1. Øresund

For PODMLP, the MLP propagator has two hidden layers of dimension 115, corresponding to the output dimension from the autoencoder. For the KAE, the state autoencoder is linear, while the forcing autoencoder is non-linear. The encoder layers have dimension 120, 120, 50.

Table B.10: Hyper-parameters for each surrogate for the Øresund case.

		PODLRt	PODMLP	LKAE	KAE
Simple	Batch size	40	40	256	128
	Optimizer	Adam	Adam	Adam	AdamW
	Optim. LR	10^{-3}	10^{-3}	10^{-3}	$1.4 \cdot 10^{-4}$
	Optim. W.D.	0	0	0	10^{-4}
	LR sche. pat.	10	10	10	10
	LR sche. fac.	0.1	0.1	0.1	0.5
	Early stop. tol.	10^{-2}	10^{-3}	10^{-2}	10^{-2}
	Early stop pat.	20	40	30	40
Eig	Batch size	40	-	256	128
	Optimizer	Adam	-	Adam	AdamW
	Optim. LR	10^{-3}	-	10^{-3}	$1.4 \cdot 10^{-4}$
	Optim. W.D.	0	-	10^{-4}	10^{-4}
	LR sche. pat.	10	-	10	10
	LR sche. fac.	0.1	-	0.1	0.5
	Early stop. tol.	10^{-2}	-	10^{-2}	10^{-2}
	Early stop pat.	20	-	30	40
TU	Batch size	128	64	64	128
	Optimizer	Adam	Adam	Adam	AdamW
	Optim. LR	10^{-2}	$3 \cdot 10^{-3}$	10^{-3}	10^{-3}
	Optim. W.D.	0	0	10^{-5}	10^{-4}
	LR sche. pat.	10	10	10	10
	LR sche. fac.	0.1	0.1	0.1	0.5
	Early stop. tol.	10^{-4}	$5 \cdot 10^{-4}$	10^{-4}	10^{-2}
	Early stop pat.	20	40	30	40
	TU steps	10	9	10	10
	TU win. stride	4	3	4	4

Appendix B.2.2. Southern North Sea

For PODMLP, the MLP propagator has two hidden layers of dimension 70, corresponding to the output dimension from all autoencoders ($20+20+10+10+10$). For LKAE and KAE, the autoencoders are concatenated with latent dimension of 40 for the states and of 30 for the forcings. For the KAE, the state autoencoder is linear, while the forcing autoencoder is nonlinear with encoding layers of size 420, 420, 420, and 30.

Table B.11: Hyper-parameters for each surrogate for the Southern North Sea case.

		PODLRt	PODMLP	LKAE	KAE
Simple	Batch size	40	40	256	256
	Optimizer	Adam	Adam	Adam	AdamW
	Optim. LR	10^{-3}	10^{-3}	10^{-4}	$1.5 \cdot 10^{-3}$
	Optim. W.D.	0	0	10^{-4}	10^{-4}
	LR sche. pat.	10	10	10	10
	LR sche. fac.	0.1	0.1	0.1	0.1
	Early stop. tol.	10^{-2}	10^{-2}	10^{-2}	10^{-2}
	Early stop pat.	20	40	30	30
Eig	Batch size	40	-	256	256
	Optimizer	Adam	-	Adam	AdamW
	Optim. LR	10^{-3}	-	10^{-4}	$1.5 \cdot 10^{-3}$
	Optim. W.D.	0	-	10^{-4}	10^{-4}
	LR sche. pat.	10	-	10	10
	LR sche. fac.	0.1	-	0.1	0.1
	Early stop. tol.	10^{-2}	-	10^{-2}	10^{-2}
	Early stop pat.	40	-	30	30
TU	Batch size	64	64	20	20
	Optimizer	Adam	Adam	Adam	AdamW
	Optim. LR	10^{-2}	10^{-3}	10^{-2}	10^{-2}
	Optim. W.D.	0	0	10^{-5}	10^{-5}
	LR sche. pat.	10	10	10	10
	LR sche. fac.	0.1	0.1	0.1	0.1
	Early stop. tol.	10^{-3}	10^{-3}	10^{-3}	10^{-3}
	Early stop pat.	40	40	30	30
	TU steps	12	12	12	12
	TU win. stride	4	4	4	4

Appendix B.2.3. Adriatic Sea

For PODMLP, the MLP propagator has two hidden layers of dimension 130, corresponding to the output dimension from all autoencoders (10+50+10+60). For the KAE, the state autoencoders are linear, while the forcing autoencoder for the BC is linear and for wind and air pressure it is nonlinear with encoding layers of size 910, 910, 910, 60.

Table B.12: Hyper-parameters for each surrogate for the Adriatic Sea case.

		PODLRt	PODMLP	LKAE	KAE
Simple	Batch size	40	128	128	128
	Optimizer	Adam	Adam	AdamW	AdamW
	Optim. LR	$7 \cdot 10^{-3}$	$7 \cdot 10^{-3}$	$5 \cdot 10^{-3}$	$4.2 \cdot 10^{-4}$
	Optim. W.D.	0	0	10^{-6}	10^{-6}
	LR sche. pat.	10	10	10	10
	LR sche. fac.	0.1	0.1	0.5	0.5
	Early stop. tol.	10^{-5}	10^{-5}	10^{-2}	10^{-2}
	Early stop pat.	20	40	50	50
Eig	Batch size	40	-	128	128
	Optimizer	Adam	-	AdamW	AdamW
	Optim. LR	$7 \cdot 10^{-3}$	-	$5 \cdot 10^{-3}$	$4.2 \cdot 10^{-4}$
	Optim. W.D.	0	-	10^{-6}	10^{-6}
	LR sche. pat.	10	-	10	10
	LR sche. fac.	0.1	-	0.5	0.5
	Early stop. tol.	10^{-5}	-	10^{-2}	10^{-2}
	Early stop pat.	20	-	50	50
TU	Batch size	40	64	64	64
	Drop out rate	-	0.3	-	-
	Optimizer	Adam	Adam	AdamW	AdamW
	Optim. LR	$6 \cdot 10^{-3}$	10^{-4}	10^{-4}	10^{-4}
	Optim. W.D.	0	0	10^{-3}	10^{-3}
	LR sche. pat.	10	10	10	5
	LR sche. fac.	0.1	0.5	0.5	0.5
	Early stop. tol.	$8.5 \cdot 10^{-5}$	10^{-5}	10^{-2}	10^{-2}
	Early stop pat.	30	40	50	50
	TU steps	10	10	10	10
	TU win. stride	5	3	4	4

Appendix C. Results

The main text shows results mainly for the surface elevations. This appendix shows the complementary figures for the other two state variables, u- and v-components of the current velocities.

Appendix C.1. Surrogate model comparisons

Figure C.12 shows the relative RMSEs for all surrogate models for U, whereas Figure C.13 shows the errors for V. As stated in the main text, the conclusions are the same for these state variables: KAE (TU) performs best for Øresund, LKAE (TU) performs best for Southern North Sea and Adriatic Sea. The main difference from figure 8 is that the temporal unrolling does not destroy accuracy of KAE in Adriatic Sea case.

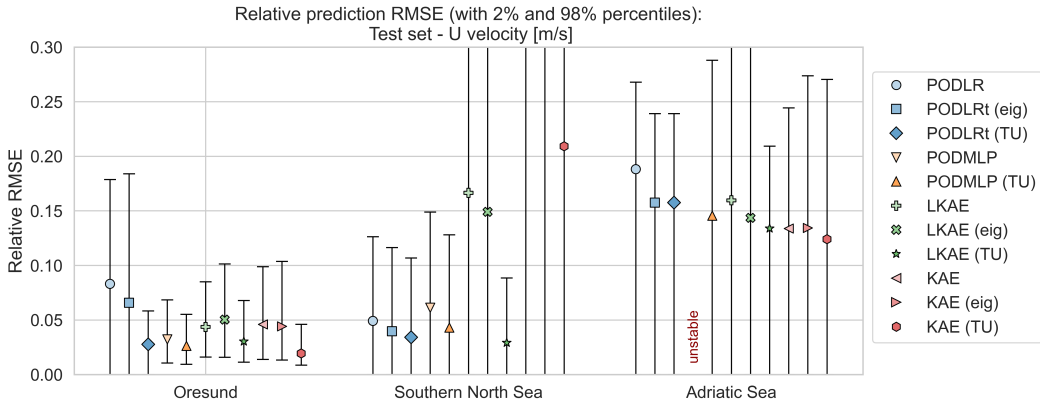


Figure C.12: Test RMSE relative to the range of values of the variable. The bars represent the 5% and 95% percentiles of the absolute errors.

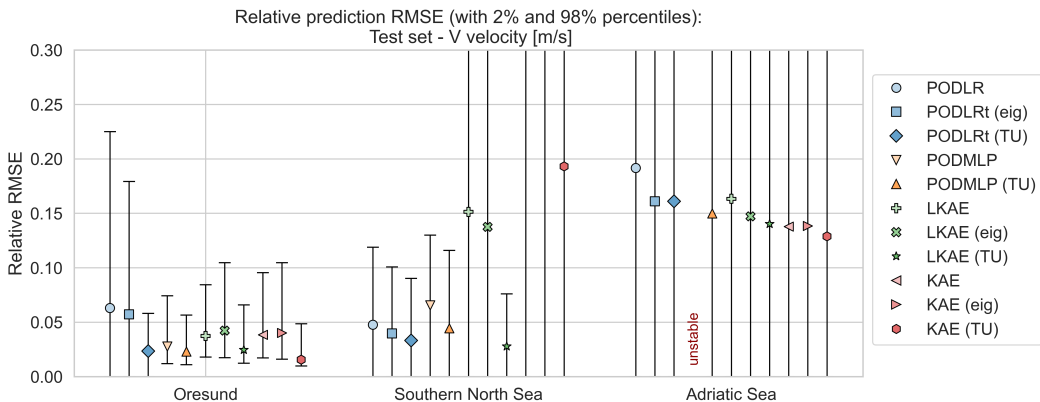


Figure C.13: Test RMSE relative to the range of values of the variable. The bars represent the 5% and 95% percentiles of the absolute errors.

Appendix C.2. Scatter plots

Figures C.14, C.15 and C.16 show the scatter plots of the predictions in the test period for the U and V variables. The conclusions are mainly the same as for the surface elevations. Some differences include that the surrogate for Øresund slightly under-estimates large U -values and slightly over-estimates small V -values. For Adriatic Sea, the predictions are further from the 1:1 line, indicating a worse fit of the current velocities than of the surface elevations.

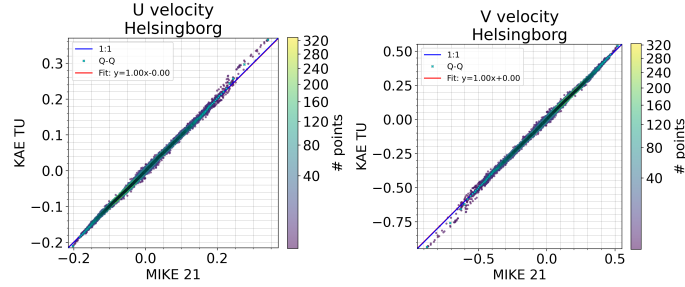


Figure C.14: Scatter plots of the simulation data (x-axis) vs. the surrogate predictions (y-axis) in the test period. U and V for the Øresund case.

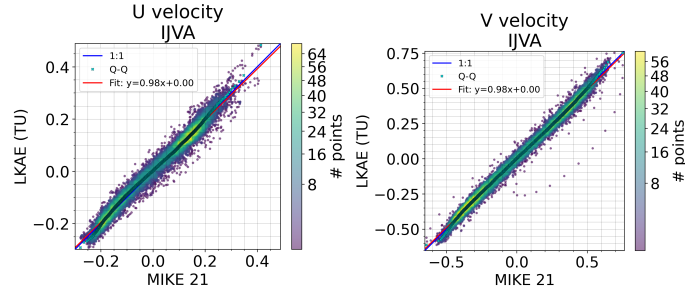


Figure C.15: Scatter plots of the simulation data (x-axis) vs. the surrogate predictions (y-axis) in the test period. U and V for the Southern North Sea case.

Appendix C.3. Spatial RMSEs

Figure C.17 and C.18 show the spatial RMSEs for U and V, respectively. The conclusions from these figures are similar to those of the surface elevations.

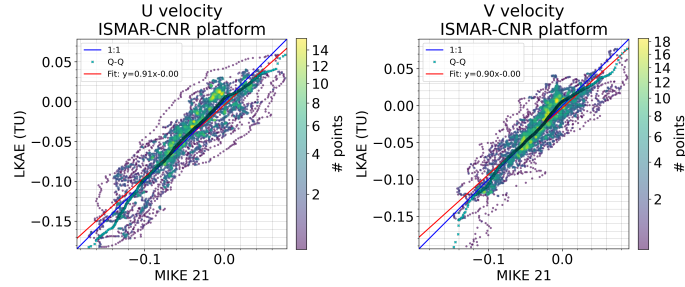


Figure C.16: Scatter plots of the simulation data (x-axis) vs. the surrogate predictions (y-axis) in the test period. U and V for the Adriatic Sea case.

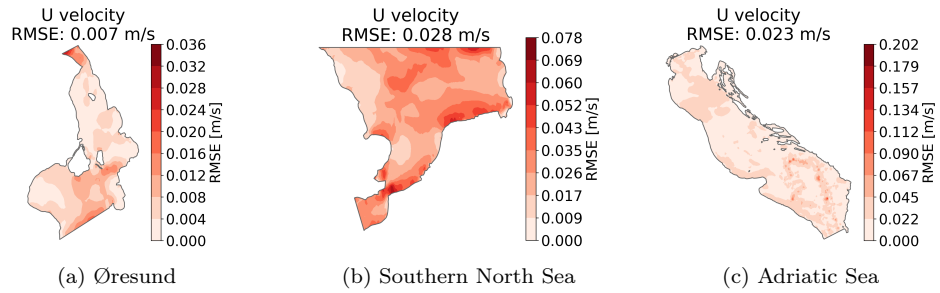


Figure C.17: Spatial RMSEs across the test period of the u-component of the current velocities.

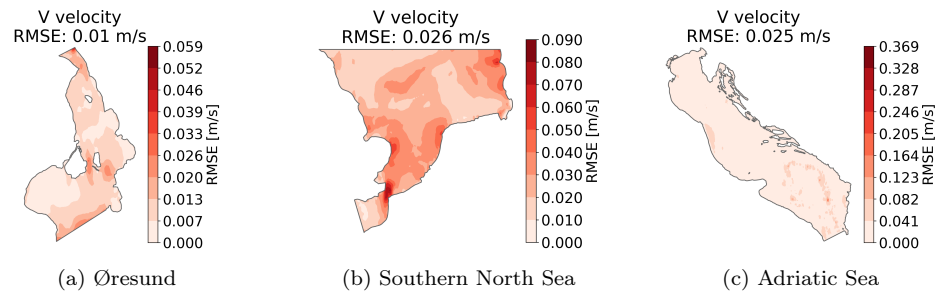


Figure C.18: Spatial RMSEs across the test period of the v-component of the current velocities.